

Title: “*Detecting the Onset and Progression of Spinodal Decomposition using Transient Grating Spectroscopy*”

Authors & affiliations:

Maxwell Rae^a, Merrill Chiang^a, Mahmudul Islam^a, Angus P. C. Wylie^b, Avery Nguyen^b,
Myles Stapelberg^b, Saleem A. Al Dajani^c, Kristýna Repček^d, Tomáš Grabec^d, Abby
Kaplan^a, Rodrigo Freitas^a, Michael P. Short^b

^aDepartment of Materials Science and Engineering, Massachusetts Institute of Technology,
Cambridge, MA 02139, USA

^bDepartment of Nuclear Science and Engineering, Massachusetts Institute of Technology,
Cambridge, MA 02139, USA

^cDepartment of Civil and Environmental Engineering, Massachusetts Institute of Technology,
77 Massachusetts Avenue, Cambridge, MA, 02139, United States of America

^dThe Institute of Thermomechanics of the Czech Academy of Sciences, Dolejškova 1402/5,
Praha 8, ZIP code 182 00, Czech Republic.

Corresponding author: Maxwell Rae (mraechu@mit.edu)

Abstract: Spinodal decomposition can degrade corrosion resistance and embrittle materials. The ability to quickly, conclusively, and non-destructively detect the onset of spinodal decomposition before catastrophic materials degradation would represent a significant advance in materials testing. We demonstrate that spinodal decomposition can be detected in binary Fe-Cr alloys via modulus stiffening using *in situ* and *ex situ* transient grating spectroscopy (TGS). The key mechanistic insight is the non-linearity in elastic moduli as function of Cr content renders a spinodally decomposed Fe-Cr alloy stiffer than an equivalent solid solution for a certain range of initial chromium compositions. We confirm the presence of spinodal decomposition in the 36 at.% chromium alloy using differential scanning calorimetry (DSC), linked to known spinodal decomposition energetics, and show via atomistic simulations that elastic modulus stiffening is expected after spinodal decomposition in the 36 at.% chromium alloy. The results of this study suggest the potential use of TGS as a practical tool for non-destructive evaluation of key materials susceptible to such degradation.

Keywords: Spinodal decomposition, transient grating spectroscopy, in-situ elastic property measurement, elastic moduli, spinodal stiffening

1. Introduction

Spinodal decomposition is a continuous phase transformation that can embrittle materials and limit the service lifetime of critical engineering components. During spinodal, a solid solution decomposes into two phases via composition fluctuations that lower the free energy of the system. In general, phase transformations in metal alloys can be categorized by degree and extent, where degree is the concentration difference across a phase boundary, and extent is the transformed volume fraction of the initial solid solution [1]. Spinodal phase transformations are initially small in degree, but large in extent—in direct contrast to nucleation and growth phase transformations, which are initially large in degree but small in extent [1]. Spinodal decomposition can have drastic effects on engineering materials. In duplex cast austenitic stainless steel (CASS) alloys, the ductile-to-brittle transition temperature (DBTT) of an in-service component operated at 400°C can shift to room temperature within two months

[2]. In addition, spinodal decomposition into α and α' phases within the δ -ferrite phase of the duplex steel causes significant chromium depletion in the α' phase, which degrades corrosion resistance [3]. Currently, no non-destructive methods exist to quantify the degree of spinodal decomposition in a component during operation.

Iron-chromium alloys are a useful system to model spinodal decomposition in the chromium enriched δ -ferrite phase of duplex stainless steels (DSS). Though nickel is a major alloying element in DSS alloys, it is not necessary for spinodal decomposition—the simplest model alloy for δ -ferrite is binary iron-chromium. Embrittlement via spinodal decomposition in the δ -ferrite phase of duplex stainless steels is a well-known life-limiting phenomenon, and literature contains extensive experimental evidence for spinodal decomposition across a range of iron-chromium compositions for temperatures at or below 500°C.

Spinodal decomposition can be characterized at the nanoscale using atom probe tomography (APT) or scanning transmission electron microscopy (STEM) to see small composition fluctuations associated with phase separation [4–7]. Xiong et al. and Miller et al. performed aging experiments at 500°C across a range of chromium concentrations to identify the chromium composition where the phase transition mechanism changes from nucleation and growth to spinodal decomposition [8–10]. Small-angle neutron scattering (SANS) has also been used to study iron-chromium phase separation [7,11]. At the microscale, hardness measurements can be used to track changes hardening due to spinodal decomposition [12]. The macroscale effects of spinodal decomposition are often characterized by Charpy impact or fracture toughness testing [13]. In the iron-chromium system, temperature and chromium composition determine the phase transformation mechanism.

All aging experiments in this study are conducted at or near 500°C on two different iron-chromium alloys. At this temperature, there is disagreement in the literature regarding the composition inside the miscibility gap that delineates nucleation and growth from spinodal decomposition. Strong evidence from SANS and APT indicate that nucleation and growth is the phase transition mechanism at and below a chromium composition of 25 at. % [8,11] and also strong evidence from SANS, STEM, and APT that spinodal decomposition is the phase transition mechanism above 35 at. % chromium [4,8,11]. Between these two compositions, the dominant mechanism remains disputed [8]. It should be noted that, due to the shape of the miscibility gap, spinodal decomposition can occur at lower chromium compositions at lower temperatures, which explains why spinodal decomposition is seen in CASS alloys. More recent literature has proposed transient grating spectroscopy (TGS) as a method for in-situ and ex-situ measurement of spinodal decomposition via elastic wave speed measurements [14].

TGS is a laser-based spectroscopic technique in which two pump lasers are crossed at the sample surface to generate a spatially dependent intensity pattern on the surface of a reflective material. This intensity profile establishes a corresponding spatial temperature profile, which launches two counter-propagating surface acoustic waves along the sample surface. While the pulsed pump laser periodically excites the sample surface, two continuous probe lasers are focused inside the pump spot to monitor the dynamics of the sample surface. The probe laser is modulated by an opaque chopper wheel to minimize sample heating. The time-dependent intensity of the probe beam reflected off the sample surface is fit to a model to determine the elastic and thermal properties of the material to a micron-scale depth below the illuminated region [15].

One TGS trace (which consists of an average of ~10,000 measurements) can be used to determine the elastic wave speed in a material along a single crystal direction, which nominally depends on the relative angle between the illuminated grain's crystal orientation and the orientation of the transient grating formed on the sample surface. For polycrystalline materials with grains larger than the spot size of the TGS probe laser (~100 μm in this work), the elastic wave speed in a given crystal direction depends on the material's density and

elastic stiffness tensor, both of which can vary with temperature and other intensive variables [16]. TGS can be used as an ex-situ or in-situ method. Ex-situ TGS involves taking a set of TGS measurements after various experimental treatments to compare thermoelastic properties as a function of experimental treatment condition. In some cases, rotation studies are done ex-situ on single crystals (or single grains in a polycrystal) to enable back-calculation of elastic constants from fitting the angular dispersion of SAW speed measurements. In-situ TGS, by contrast, involves taking TGS measurements continuously as a function of some treatment (e.g. time at temperature).

Previous work by Al Dajani et al. showed, via molecular dynamics simulations, that iron-chromium de-mixing—analogous to spinodal decomposition—stiffens the elastic modulus of iron-chromium alloys [14]. The same study also predicted surface acoustic wave (SAW) and pseudo surface acoustic wave (PSAW) speeds in duplex CASS alloys, and subsequently measured SAW and PSAW speeds in samples without spinodal decomposition in the δ -ferrite phase. Samples exhibiting spinodal decomposition supported elastic waves faster than those allowed by the computed elastodynamic function at any orientation. The authors hypothesized that spinodal decomposition stiffened the δ -ferrite phase, causing the speed of a subset of the measured elastic waves to increase into the elastodynamically unallowed region [14]. In addition to producing waves in the unallowed region, aged samples also showed a higher incidence of “peak splits”, where two acoustic modes are supported in the same measurement. The higher incidence of peak splitting was attributed to the stiffening effect of spinodal decomposition on the δ -ferrite phase in the duplex stainless steel, which widened the average gap in elastic wave speed between acoustic modes in austenite and δ -ferrite phases [14].

The work of Al Dajani et al. used TGS on CASS alloys to measure changes in elastic wave speed as a function of time at temperatures where spinodal decomposition is known to occur (10,000-30,000 hours at 290-400°C) [14]. However, the absolute effect of spinodal decomposition on elastic modulus could not be completely disentangled from material stiffening by other mechanisms (e.g., G-phase precipitation), because CASS alloys are complex engineering materials with multiple alloying elements and a complex microstructure [14]. In addition, reproducing the peak-split assessment from the open data repository of ref 14 is challenging because noise in the power spectrum of the TGS trace is difficult distinguish from peaks due to acoustic modes. Reassessment is made possible by the existence of the open data repository, which the authors should be commended for. However, without a consistent and reliable means of differentiating signal from noise in the power spectrum, experimenter bias in labeling will hinder the reliability of peak-split assessments. Finally, the effect of spinodal decomposition on the elastic constants of the medium could not be measured experimentally in CASS, because the crystal orientation relative to the TGS grating was not controlled, and the δ -ferrite grains in the CASS alloy were smaller than the spot size of the TGS probe laser [14].

In this work, the effect of spinodal decomposition on elastic modulus of two iron-chromium alloys is measured using ex-situ and in-situ experimental methods and molecular dynamics simulations. The binary nature of the system mitigates complicating effects such as G-phase precipitation, which requires additional alloying elements such as nickel. The ex-situ TGS rotation study further controls for the influence of crystal orientation on SAW speed, enabling direct measurement of the effect of thermal aging on the angular SAW dispersion. The presence of spinodal decomposition in the heat-treated alloy is substantiated by differential scanning calorimetry (DSC). Finally, the value of TGS as a non-contact, non-destructive method to measure spinodal decomposition is demonstrated, and future technologies leveraging TGS are discussed.

2. Methods

2.1 Sample Preparation and Aging Conditions

The Fe-36Cr sample (see Table 1) was prepared using a Centorr arc melter with a tungsten electrode under an argon environment. The chamber was evacuated and flushed with argon 10 times prior to each melt, and the alloy was flipped and re-melted 3 times to improve compositional homogeneity. A ~20-gram sample was made with 3.2-6.4 mm irregularly shaped 99.99% pure iron pieces and 2-3 mm irregularly shaped 99.995% pure chromium pieces from BeanTown Chemical. The Fe-26Cr alloy came from a historical sample and its method of production is not known, but homogenization and subsequent composition measurements enable the Fe-26Cr alloy used in this study to be reproduced by any number of methods. Samples were sectioned with a diamond saw to ~2 mm thick, and ~100 mL of Kalling's reagent number 2 (Aqua Solutions, catalog number SPX440) was used to etch the sample for ~90 seconds. Kalling's reagent number 2 is a mixture of ethanol (~90 wt. %), copper (II) chloride (~3 wt. %), hydrochloric acid (~5 wt. %), methanol (~1 wt. %), and isopropyl alcohol (~1 wt. %). This revealed the grain microstructure, and a grain with a minimum dimension larger than 200 μm was selected in the Fe-36Cr and Fe-26Cr alloys by marking with a razor blade. Selective grain marking was done on the sample stage of a Zeiss ML-100 optical microscope, to facilitate identification of a large grain.

Alloy heat treatments were done using an MTI KSL-1200X annealing furnace. Samples were drop-quenched in deionized (DI) water from VWR Analytical (catalog number BDH1168-5GL, $< 1 \mu\text{S}/\text{cm}$, $< 50 \mu\text{g}/\text{L}$ organic carbon, $< 5 \mu\text{g}/\text{L}$ sodium, $< 5 \mu\text{g}/\text{L}$ chlorides, $< 3 \mu\text{g}/\text{L}$ total silica) after each heat treatment, and any oxidation was polished off the sample before TGS measurement using 800 and 1200 grit SiC sandpaper, then 3-, 1-, 0.25-, and 0.1- μm diamond solutions, followed by a 0.05- μm OPS alumina polish. Homogenization and subsequent heat treatments were done in air in a KSL-1200X muffle furnace with 0.1°C temperature control accuracy achieved using a Eurotherm temperature controller. Both alloys underwent the same homogenization treatment at $1000 \pm 0.1^\circ\text{C}$ in air for 2 hours, followed by a drop quench in DI water. Subsequent heat treatment procedures were performed at $500 \pm 0.1^\circ\text{C}$, also followed by drop quenching in DI water. A final re-homogenization was performed on the Fe-36Cr alloy for 1 hour at $1000 \pm 0.1^\circ\text{C}$, followed by a drop quench in DI water. After the initial homogenization, and in between each heat treatment, TGS measurements were taken. Alloy compositions were measured by inductively coupled plasma optical emission spectroscopy (ICP-OES) with a detection limit of 100 parts per million for trace metals, results for this analysis are shown in Table 1.

Alloy Name	Fe [at. %]	Cr [at. %]	Trace Elements [at. %]
Fe-26Cr	73.9	26.1	0.012 (Ti), <0.01 (All other)
Fe-36Cr	63.7	36.3	<0.01 (All)

Table 1. Alloy compositions measured by ICP-OES with ASTM E 1479-16.

2.2 Electron Backscatter Diffraction Measurements

Electron backscatter diffraction (EBSD) measurements were done on a JEOL JSM 7900F Schottky FE-SEM at 20 keV using an Oxford Symmetry EBSD detector with a probe current of ~156 μA . Aztec EBSD software was used to extract the Euler angles of the grain that was marked and used for TGS studies. The Euler angles relate the coordinate system of the SEM image to the crystal coordinate system of the material. A computer code was written

and used to extract the crystal surface orientation of the razor-marked grain from the set of Euler angles given by EBSD using the appropriate rotation matrix. The code used to perform this matrix algebra can be found in the data availability GitHub repository for this paper [17].

2.3 Transient Grating Spectroscopy

Two TGS instruments were used, one for ex-situ measurements at room temperature (in between heat treatments), and one for separate in-situ experiments. Ex-situ TGS measurements were done on a system described in ref. 14. In-situ measurements were done using a TGS system described in ref. 18, with in-situ heating under $< 1 \times 10^{-5}$ Torr vacuum using a HeatWave button heater (catalog number #101275-28) and continuously monitored temperature via either an in-heater or on-sample K-type thermocouple.

In the two in-situ experiments, two different temperature control methods were used. In the first experiment, a K-type thermocouple was spot-welded to the surface of the Fe-36Cr alloy, and temperature was controlled using the on-sample thermocouple. On-sample control resulted in temperatures that ranged from 498-500°C throughout the in-situ TGS experiment.

In the second in-situ experiment, an on-sample thermocouple was used for continuous monitoring, and an in-heater thermocouple was used for temperature control (both K-type thermocouples). In-heater control resulted in on-sample temperatures that ranged from 473.9-475.8°C during the first 1.7 hours of testing, after which the on-sample thermocouple disconnected, and temperature readings ceased. The in-heater thermocouple, however, remained connected and had temperature control of better than 1 °C throughout the experiment. During the 1.7 hours the on-sample thermocouple was actively taking measurements, the temperature rose steadily from 473.9°C when in-situ TGS measurements began, to 475.8°C when the on-sample thermocouple disconnected. Temperature rise was roughly logarithmic in time.

All TGS measurements were taken at a nominal grating spacing of 6.4 μm (the exact grating spacing varies experiment-to-experiment based on the location of the pump laser through the phase mask), and exact grating spacings for each experiment are indicated in the data availability repository [17].

2.4 Elastic Constant Calculation from Ex-Situ TGS Data

A subset of the independent elastic constants can be calculated by solving the so-called “inverse problem” using the SAW speed as a function of rotation angle [16]. To solve the inverse problem and compute changes in elastic constants, the sample must be a single grain with dimensions larger than the spot size of the TGS probe laser (~62 μm across) and a known surface orientation. The surface orientation of the crystal determines which crystal directions the laser-induced grating probes, and thus the elastic wave speed as a function of the physical sample orientation angle. In this work, the surface orientation of the grain used in ex-situ TGS studies was determined via EBSD. Then, using the mass density and the surface orientation of the sample, a computer code iteratively tested different sets of elastic constants to find those that minimize the sum-square deviation of the angular dispersion of SAW velocities from the measured dispersion [18]. A detailed description of the approach is provided in ref. 18.

2.5 Differential Scanning Calorimetry

DSC measurements were performed on a Netzsch 404F3 Pegasus equipped with a silicon carbide furnace (maximum temperature 1650°C) and a type-P measurement head (maximum temperature 1150°C) for improved response at lower temperatures. DSC

measurements were done under 99.999% argon cover gas with < 1 ppm oxygen impurities using a zirconium getter ring. For the validation test, two samples of Fe-36Cr aged at 500°C for 10 hours were measured. Samples were placed in manufacturer-provided alumina crucibles with lids. The temperature program consisted of five heating and cooling cycles, with a maximum temperature of 700°C (chosen to be above the approximate critical temperature of the spinodal phase transformation $T_{SP} \sim 627^\circ\text{C}$) [19]. Dynamic steps were performed at a heating/cooling rate of 10°C/min, with an isothermal segment of 30 minutes at the minimum temperature of 100°C to allow thermal stabilization. The time-temperature history of DSC measurements is illustrated in Fig. 1. To calibrate the instrument for the particular configuration of these experiments, corrections (e.g. measurements of the empty crucibles) were performed, as well as a measurement of a sapphire heat capacity standard in the temperature range of interest. A comprehensive description of calibration and corrections in DSC measurements are provided in the supplementary materials of ref. 20, which were closely followed here [20].

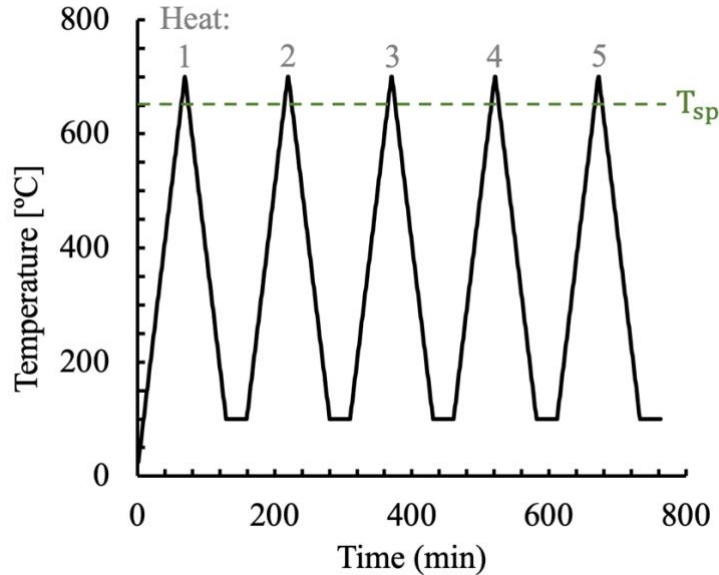


Figure 1. DSC heating profile. Heat 1 raises the sample above the spinodal temperature (to mix the decomposed phases into a single solid solution), and Heats 2-5 serve as annealed baseline measurements.

Because the enthalpy change of iron and chromium de-mixing is weak, post-processing steps are required, such as fitting the phase transformation peak as performed in refs. 21 and 22. First, the corrections are averaged and subtracted from the measurement of the combined sample and crucibles. Next, a third-order polynomial is fit to the DSC data outside of the region of interest for the phase transformation. A third-order polynomial fits the data well and is consistent with a heat capacity that depends only weakly on temperature beyond its second-order term. The region of interest for the phase transformation is 500°C - 625°C, based on the aging temperature, peak width, and heating rate combinations reported in other studies of unmixing [21,22]. The polynomial baseline is then subtracted from the DSC data. Next, since separation of phases formed during aging will only occur in the first heating step, the subsequent heats (two through five) are averaged across the two measured samples, to provide an “as-unmixed” value. Finally, the average of the first heating steps is taken, and the subsequent heating steps are subtracted, yielding a curve representing only the heat flow unique to the first heat.

2.6 Atomistic Simulations

Hybrid molecular dynamics/Monte Carlo (MD/MC) simulations were performed using the Large-scale Atomic/Molecular Massively Parallel Simulator (LAMMPS) [23] to thermally equilibrate the Fe-Cr system, effectively replicating the heat treatment process conducted experimentally. A body-centered cubic (BCC) cell was first initialized by randomly distributing Fe and Cr atoms according to either the 26 or 36 at. % Cr composition. The system was oriented such that the $\langle 100 \rangle$ crystallographic directions aligned with the x, y, and z axes of the simulation cell. The simulation box dimensions were $13.6 \text{ nm} \times 13.6 \text{ nm} \times 13.6 \text{ nm}$, containing 207,646 atoms. These dimensions were chosen to be sufficiently large to accommodate the experimentally observed spinodal decomposition wavelength of 4.5 nm [7]. Periodic boundary conditions were applied in all three directions, and atomic interactions were modeled using an embedded-atom method (EAM) interatomic potential [24].

The system was initially relaxed at 773 K and zero pressure using a Nosé–Hoover thermostat and barostat, both with a damping parameter of 1 ps and chain length of 3. Subsequently, MC swap attempts were introduced between atoms of different elements, with swaps accepted or rejected based on the Metropolis criterion [25,26]. This probabilistic rule accepts swaps that lower the system energy or, alternatively, accepts energy-increasing swaps with a probability of $\exp(-\Delta E/k_B T)$, where ΔE is the change in system energy, k_B is the Boltzmann constant, and T is the temperature (set to 773 K). Each MC step consisted of 10 attempted atom swaps, followed by 10 ps of MD relaxation at 773 K. A timestep of 1 fs was used for the MD steps. A total of 200,000 MC steps were performed to ensure full equilibration of the structure (equivalent to a total of 10 MC steps per atom). To ensure statistical robustness, the simulation was repeated 10 times with different initial random configurations.

The elastic constants of both the random and thermally equilibrated systems were evaluated by measuring changes in the average stress tensor in response to finite deformations of the simulation cell volume [27] at 300 K. Elastic constants C_{11} , C_{12} , and C_{44} represent the computed components of the stiffness tensor in Voigt notation. All atomistic simulation visualizations were performed using the Open Visualization Tool (OVITO) [28].

The characteristic wavelength and amplitude of spinodal decomposition were quantified by analyzing concentration profiles along x-direction at multiple (y,z) locations within the simulation box. The wavelength was determined from the first nontrivial peak of the autocorrelation function of the concentration profile, which captures the dominant repeat distance of compositional fluctuations [5,29,30]. The amplitude was obtained by fitting the distribution of local concentrations to the Langer-Bar-on–Miller two-Gaussian mixture probability density function, thereby extracting the peak-to-trough composition contrast [31,32]. To account for statistical variation across different sampling locations and independent simulation runs, the median values of both wavelength and amplitude were reported, with associated uncertainties defined as half the interquartile range.

3. Results

3.1 Microstructural Characterization

After the samples were prepared and single grains within each sample were marked, EBSD was performed on the marked region for the Fe-36Cr sample only. The sample preparation method is shown in Fig. 2. EBSD was used to determine the surface orientation of the marked grain. The $[\phi_1, \Phi, \phi_2]$ Euler angles from the Aztec software Kikuchi band fitting algorithm were used to calculate the surface orientation of the razor-marked grain. For Euler angles of [1.2878, 0.6795, 0.9328] radians, the surface orientation of the razor-marked grain in the Fe-36Cr sample was found to be [0.5048, -0.3743, 0.7779] radians. The surface orientation

was then used to solve the inverse problem to extract changes in elastic constants as a function of time-at-temperature.

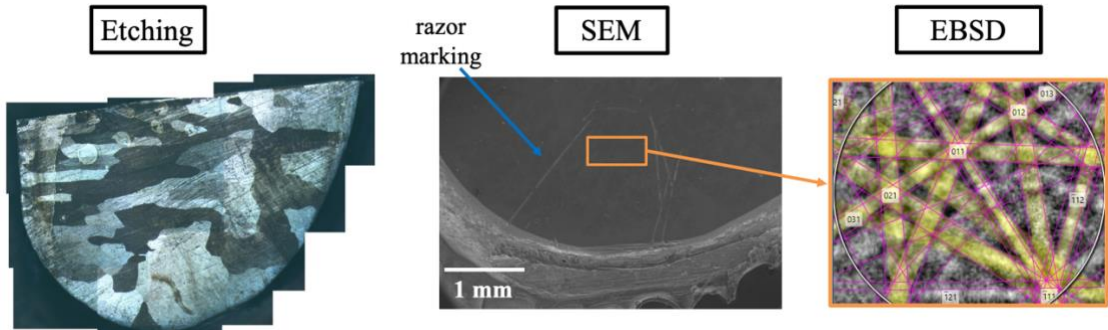


Figure 2. From left to right: Fe-36Cr alloy after etching to reveal grain structure (optical image), after razor marking and re-polishing (SEM image), and an electron backscatter diffraction pattern.

3.2 TGS Ex-situ Analysis

TGS results on the Fe-36Cr and Fe-26Cr alloys will be presented first, followed by calculation of the change in the elastic constants of the Fe-36Cr alloy as a function of heat treatment condition. The various heat treatments are described in the Methods section and summarized in Table 2 below. Table 2 also includes a column for the average SAW speed around a relative minimum of the angular SAW dispersion. The decision to highlight a relative minimum in the SAW dispersion is based on prior literature showing that spinodal decomposition is preferentially modulated along elastically soft directions [33]. Later, these results will be discussed in the context of spinodal decomposition in elastically anisotropic media. Figure 3 shows the time-temperature history of Fe-36Cr and Fe-26Cr aging, along with the relative minimum SAW speed for the Fe-36Cr alloy as a function of heat treatment condition.

The SAW speeds at the relative minima for the Fe-36Cr alloy were measured at 36° relative rotation. The standard deviation in a SAW speed measurement was computed using 10 TGS measurements at different areas within a single grain at one relative rotation angle. The error in the power spectrum frequency fit used to find the SAW speed was computed, but in every case it was found to be approximately two orders of magnitude smaller than the variance in the measurement, and was therefore not propagated. The same method was used to compare SAW speeds near a relative minimum (~36 degrees in Fig. 4) for the Fe-26Cr alloy. The angular dispersion of SAW velocities in the Fe-36Cr and Fe-26Cr alloys is shown in Fig. 4 for the conditions shown in Table 2.

Alloy	Heat Treatment	Time [hr]	Temp. [°C]	Minima SAW Speed [m/s]
Fe-36Cr	HOM1	2	1000	2703.6 ± 2.8
Fe-36Cr	HT1	1	500	2728.7 ± 3.3
Fe-36Cr	HT2	10	500	2759.4 ± 3.2
Fe-36Cr	HOM2	1	1000	2649.3 ± 2.8
Fe-26Cr	HOM1	2	1000	2750.6 ± 6.0
Fe-26Cr	HT1	20	500	2732.2 ± 5.3
Fe-26Cr	HOM2	1	1000	2735.6 ± 7.5

Table 2. Heat treatments and SAW speeds along a soft (36°) crystal direction. Errors in the minima SAW speed denote the standard deviation of three points around the relative minima.

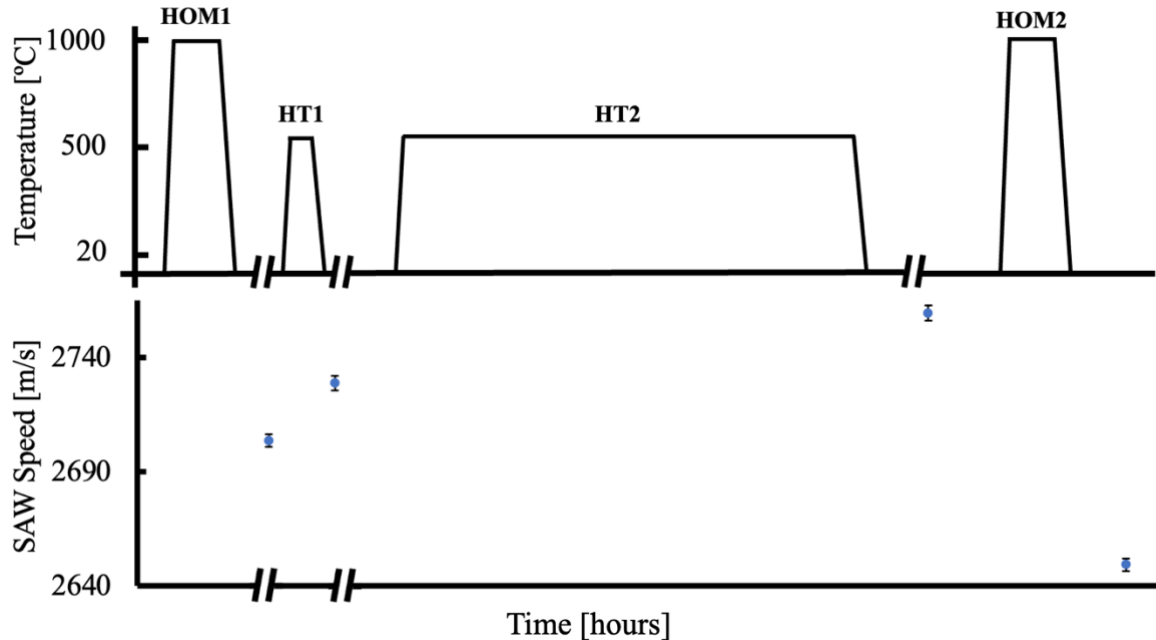


Figure 3. Top graph: pictorial representation of time-temperature processing conditions for the Fe-26Cr and Fe-36Cr alloys. Bottom graph: SAW speed at relative minima for Fe-36Cr alloy (error bars are one standard deviation above and below the mean).

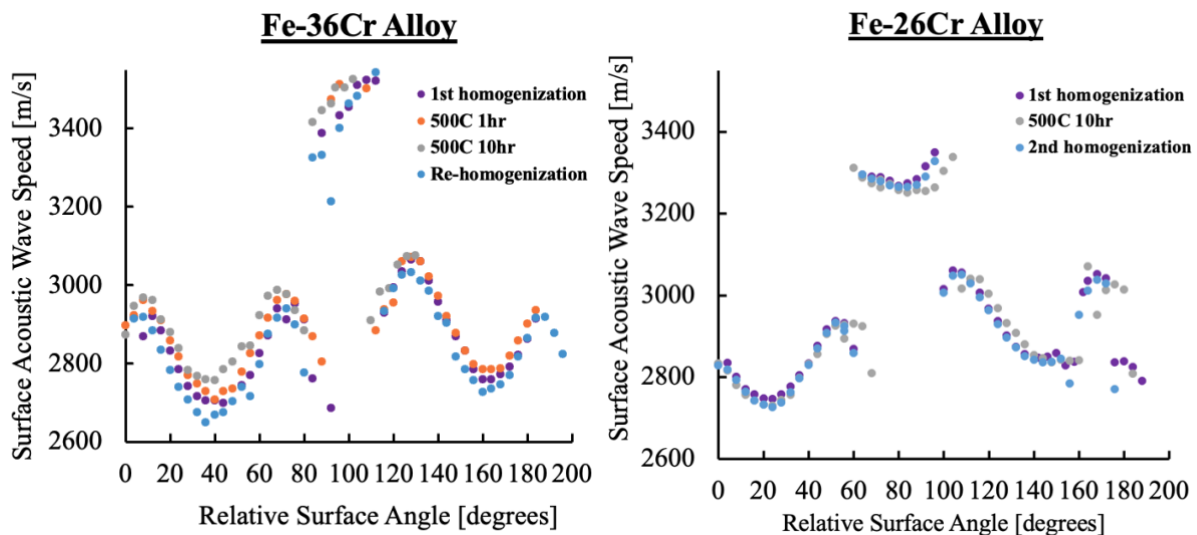


Figure 4. SAW speed as a function of relative surface angle for the Fe-36Cr and Fe-26Cr alloys—each point was taken in the same single grain after each heat treatment. The standard deviation in plotted SAW speed measurements is $\sim 0.1\%$ of the measured value, which is too small to see on the plot.

The lefthand graph in Fig. 4 shows the angular SAW dispersion for the Fe-36Cr alloy for the different heat treatment conditions tested. Using the experimentally measured angular SAW dispersions, the inverse problem was solved to compute the two independent elastic constants that produce significant out-of-plane displacement. The results are shown in Table 3. Notably, C' for both samples aged at 500°C, where spinodal decomposition is expected, is more than two standard deviations higher than either homogenized case, where spinodal decomposition is not expected.

Heat Treatment	C' [GPa]	C_{44} [GPa]	Spinodal expected?
1000°C, 2 hr	56.7 ± 0.3	113 ± 0.9	No
500°C, 1 hr	58.2 ± 0.3	114.7 ± 0.7	Yes
500°C, 10 hr	59.8 ± 0.3	111.3 ± 0.7	Yes
1000°C, 2 hr	55.0 ± 0.3	112.8 ± 1.0	No

Table 3. Elastic constants of the 36 at. % chromium alloy, found by solving the inverse problem. The relationship between C' , C_{11} , and C_{12} is $C' = 0.5(C_{11} - C_{12})$. Reported error is the 1-sigma fitting error described in ref. 18.

3.3 TGS In-situ Analysis

The second set of TGS results was obtained in-situ on the Fe-36Cr alloy. Two in-situ tests were conducted at nominal temperatures of 500°C, and 475°C (see Figure 5). In both experiments, the SAW speed increased as a function of time at temperature. Note in Fig. 5 that SAW speed stiffened in both samples during heat treatment at 475°C and 500°C (where spinodal decomposition occurs), independent of the temperature control and measurement scheme used.

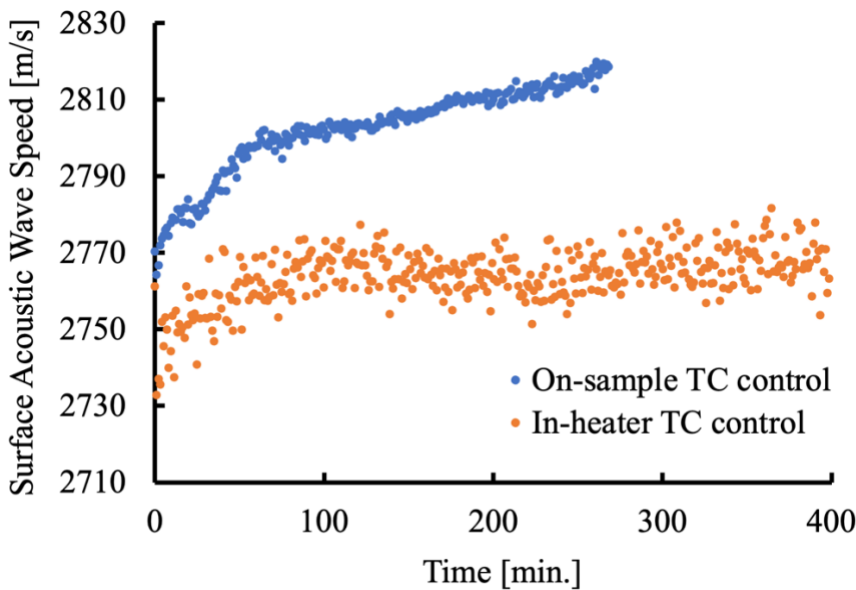


Figure 5. In-situ TGS results for Fe-36Cr for two different temperature control schemes.

In the in-situ experiments, two temperature control schemes were tested to determine which was optimal. The in-situ sample labeled “on-sample TC control” was temperature-controlled using the on-sample thermocouple, while “in-heater TC control” was controlled using the in-heater thermocouple (TC). Temperature control based on the on-sample thermocouple resulted in temperature stability within 1°C once 500°C was reached (499.8 ± 0.5 °C). By contrast, when temperature was controlled by the in-heater thermocouple, the on-sample temperature continued to rise over the course of the experiment at a rate of ~ 1.5 °C/hour (from 473.1°C to 475.8°C during the first 1.7 hours). The nominal temperature for the in-heater TC control sample was 475°C.

3.4 Differential Scanning Calorimetry

DSC is utilized as a secondary verification for whether spinodal decomposition has occurred in the Fe-36Cr alloy. Figure 6 shows the averaged first heats and the averaged subsequent heats, and Figure 7 shows the difference between the two. To extract the enthalpy, this curve is integrated over the region of interest. This yields a measured unmixing enthalpy of 27.3 ± 9.5 J/g. The peak temperature for Heat 1 is near 550°C. Errors are defined by the variance between first heats and the variance between all subsequent heats, then summed in quadrature.

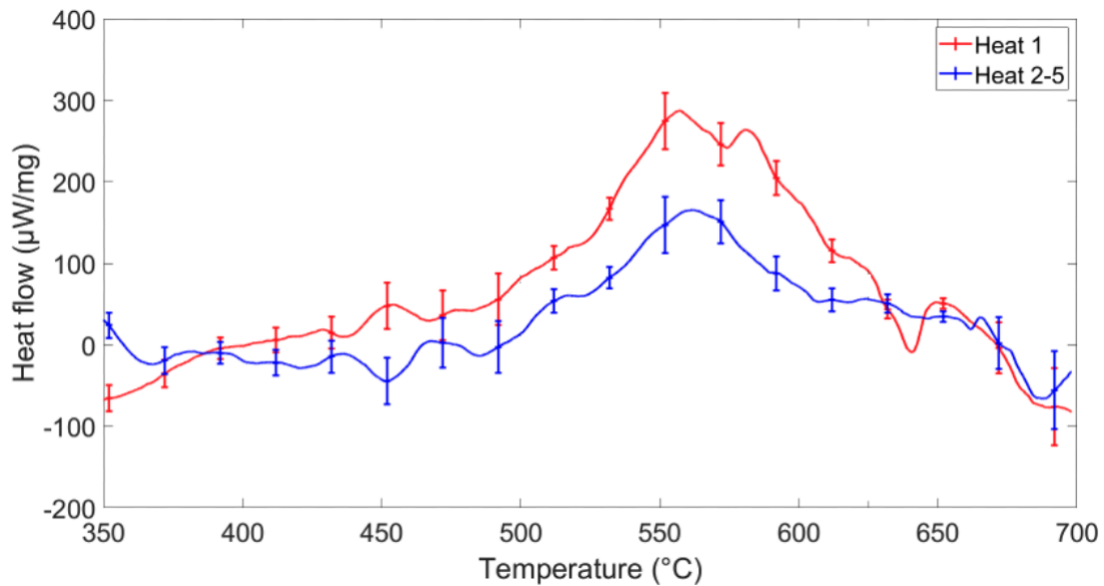


Figure 6. Heat 1 (where spinodal is expected to exist) vs. subsequent heats 2-5.

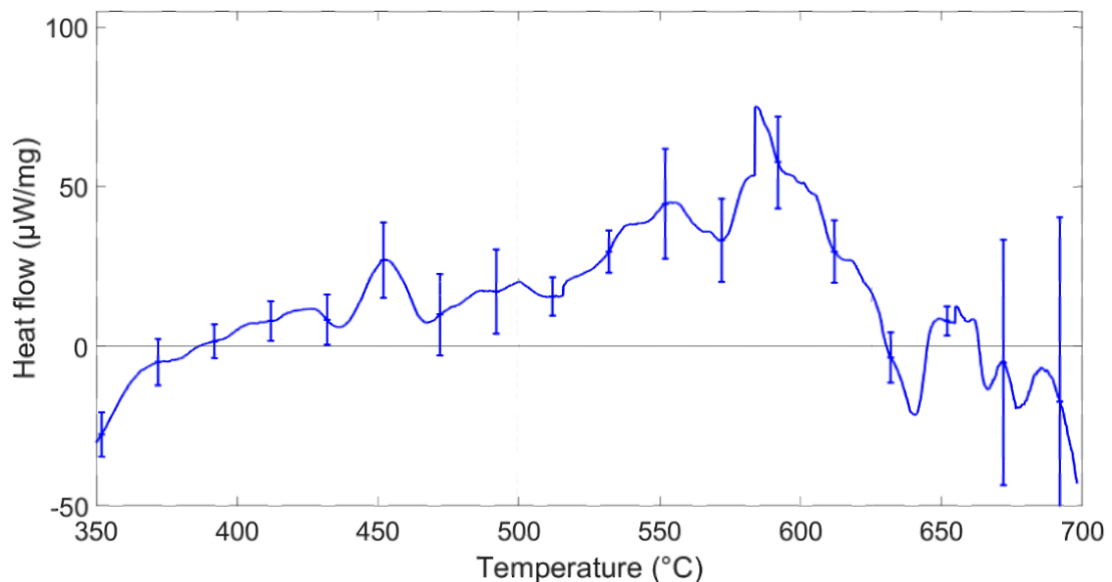


Figure 7. Difference in heat flow between 1st and subsequent heats.

3.5 Atomistic Simulations

Hybrid MD/MC simulations were performed to support the experimental analysis. Figure 8 shows the Fe-26Cr and Fe-36Cr alloys before and after thermal equilibration, revealing clear phase separation in both cases into Fe-rich and Cr-rich regions. The approach described in ref. 5 was used to calculate the spinodal decomposition wavelength and amplitude for both alloys in the thermally equilibrated state. Because the distributions of both spinodal wavelength and amplitude are skewed, the median and interquartile ranges of each are reported. The median spinodal wavelength for the Fe-26Cr and Fe-36Cr alloys were 2.75 nm and 2.89 nm, respectively, with 25th and 75th percentile ranges of 1.92-3.98 nm and 2.06-4.13 nm. The median composition amplitude (mole fraction) for the Fe-26Cr and Fe-36Cr alloys was 0.18 and 0.26, respectively, with 25th-75th percentile ranges of 0.14-0.22 and 0.21-0.32.

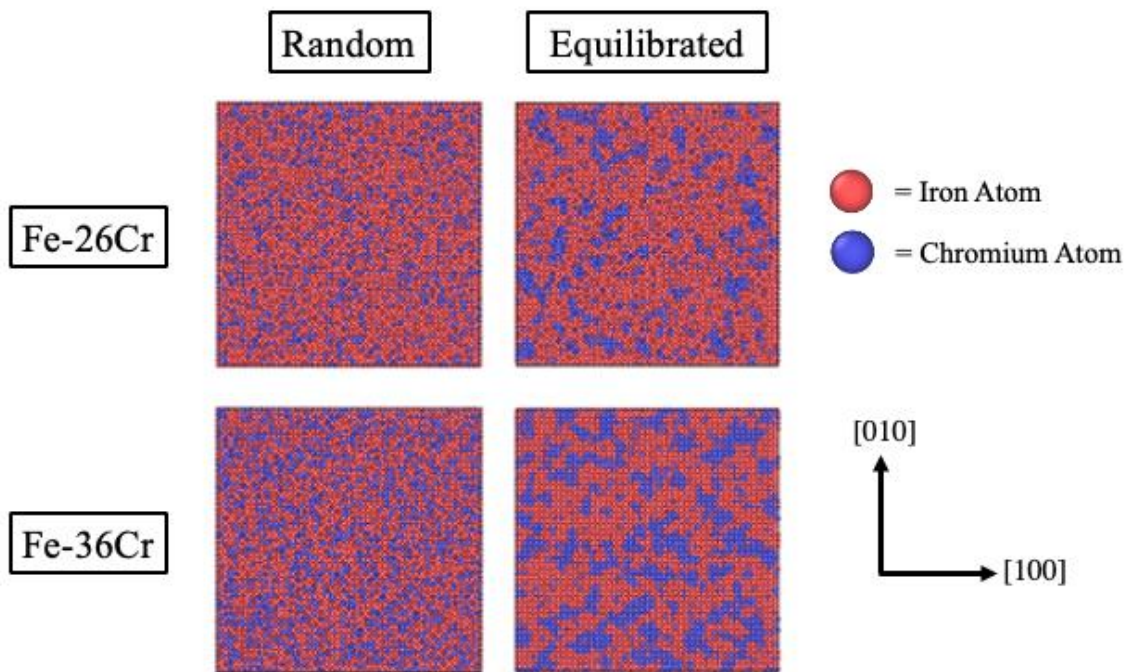


Figure 8. OVITO visualizations of Fe-26Cr and Fe-36Cr systems in the solid solution and thermally equilibrated (at 500°C) states used for elastic constant calculations.

Molecular dynamics was also used to examine changes in material properties before and after thermal equilibration at 500°C. Specifically, the elastic stiffness tensor and density were measured for both states:

$$C_{ij}^{ss} = \begin{bmatrix} C_{11} & C_{12} & 0 \\ C_{12} & C_{11} & 0 \\ 0 & 0 & C_{44} \end{bmatrix} = \begin{bmatrix} 184.77 \pm 0.13 & 102.32 \pm 0.1 & 0 \\ 102.28 \pm 0.1 & 184.77 \pm 0.14 & 0 \\ 0 & 0 & 85.52 \pm 0.05 \end{bmatrix}$$

and

$$C_{ij}^{aged} = \begin{bmatrix} 195.4 \pm 0.2 & 105.42 \pm 0.13 & 0 \\ 105.41 \pm 0.13 & 195.39 \pm 0.21 & 0 \\ 0 & 0 & 89.2 \pm 0.05 \end{bmatrix},$$

where C_{ij}^{ss} and C_{ij}^{aged} represent the elastic stiffness tensors for the solid solution and thermally equilibrated systems, respectively, in the Fe-36Cr alloy. The units for all elastic stiffness tensor components are in gigapascals. On a percentage basis, the average stiffness increases for C_{11} , C_{12} , and C_{44} , were 5.74±0.07%, 3.03±0.09%, and 4.32±0.04%, respectively. Errors represent

one standard deviation about the mean, computed from 10 independent simulations for each alloy before and after thermal equilibration. In addition to the elastic stiffness tensor, the density of the Fe-36Cr alloy in the solid solution and aged conditions was computed via MD and found to be $7367 \pm 2 \text{ kg/m}^3$ and $7444 \pm 2 \text{ kg/m}^3$.

4. Discussion

4.1 Evidence for Spinodal in the Fe-36Cr Alloy

To establish a direct link between spinodal decomposition and stiffening, evidence must be present for both effects. In the early stages of spinodal decomposition, characterizing the presence and extent of spinodal is difficult. Because the Fe-26Cr alloy did not show a significant increase in SAW speed after aging, no attempt was made to characterize phase separation. In the Fe-36Cr alloy, however, a SAW speed increase after aging was observed (see Fig. 3). To characterize spinodal decomposition in the Fe-36Cr alloy, DSC was used to measure enthalpy release upon de-mixing.

That spinodal decomposition occurs in Fe-36Cr alloys at 500°C is well established in the literature [4,8,11]—DSC was used for direct verification of phase separation in the sample used for ex-situ TGS studies. Two key features of the heat flow vs. enthalpy curve from DSC are the unmixing enthalpy, obtained by integrating over the temperature range of interest, and the peak temperature. The unmixing enthalpy and peak temperature are correlated with the amplitude and wavelength of composition fluctuations, respectively [21,22]. For the Fe-36Cr alloy aged for 10 hours at 500°C, an unmixing enthalpy of $27.3 \pm 9.5 \text{ J/g}$ and a peak temperature of $\sim 550^\circ\text{C}$ were measured. These values are in reasonable agreement with those found by Couturier et al. for much longer aging times at lower aging temperatures in an Fe-15.85Cr stainless steel [21]. The observation of a positive enthalpy release in the Fe-36Cr alloy indicates the re-solution of phase separation that occurred due to aging at 500°C. The extensive literature on similar alloys strongly supports the mechanism of phase separation is spinodal decomposition [4,8,11]. Further work could be done to characterize the nature of the decomposition in the Fe-36Cr alloy, but the focus of this work is to demonstrate the viability of TGS as a tool to study the mechanical effects of spinodal decomposition rather than the decomposition process itself. The discussion now turns to the use of ex-situ and in-situ TGS as complementary methods for measuring the effect of spinodal decomposition on elastic properties of the Fe-36 and Fe-26Cr alloys.

4.2 Ex-situ TGS Discussion

Although ex-situ TGS studies are inherently time-intensive and laborious, their use offers distinct experimental advantages that justify their application. First, the dependence of surface acoustic wave speed on crystal orientation can be controlled by selecting a single grain for study and rotating through the same set of angles after each successive heat treatment. Second, if the surface orientation of the selected grain is known, a subset of the independent elastic constants can be calculated by solving the inverse problem [18]. Both binary iron-chromium alloys used in this study consist of the α -ferrite phase, which is body-centered cubic and has three independent elastic stiffness tensor components: C_{11} , C_{12} , and C_{44} in Voigt notation. TGS is most sensitive to surface acoustic waves, which produce significant shear displacements. Consequently, only the two shear-related elastic constants can be obtained by solving the inverse problem (out of the three total independent elastic constants) [18].

In the Fe-36Cr alloy, the SAW speed as a function of rotation angle is shown in Fig. 4 for four different time-at-temperature conditions. Compared to the as-homogenized state, heat treatments of 1 and 10 hours at 500°C result in anisotropic stiffening, with greater stiffening along initially elastically soft directions (local minima in Fig. 3), as shown in Table 2. Spinodal decomposition is known to modulate along elastically soft directions in cubic alloys with negative elastic anisotropy to minimize elastic strain energy [33].

By converting the elastic constants C_{11} and C_{12} into C' using the expression in Table 3, and directly comparing C_{44} , the relative changes in elastic constants predicted by hybrid MD/MC and those measured by solving the inverse problem can be compared. In absolute terms, the values are not in close agreement; however, the relative changes due to spinodal decomposition are more significant in this context. This focus on relative rather than absolute values reflect that interatomic potentials in atomistic simulations typically capture trends in material response more reliably than exact physical constants. Although absolute elastic constants depend strongly on the potential's parameterization, relative changes across thermodynamic states—such as before and after spinodal decomposition—consistently represent the correct physical behavior. The inverse extraction of the C' elastic constant is the most precisely determined of the three independent elastic constants because the value of C' is strongly correlated with surface acoustic waves. In contrast, C_{44} depends more strongly on pseudo-surface acoustic waves, which are more difficult to evaluate from the experimental data taken in this study.

The relative change in C' after 1 and 10 hours at 500°C is $2.6 \pm 0.5\%$ and $5.4 \pm 0.5\%$, respectively. The reported uncertainty represents the error in the inverse calculation of the C' elastic constant. From hybrid MD/MC, the relative change in C' from random solid solution to the thermally equilibrated state at 500°C is $9.1 \pm 0.3\%$. The uncertainty from MD/MC corresponds to the propagated standard deviation of the ten elastic constant measurements taken before and after thermal equilibration. Thermal equilibration in MD/MC represents a long-term aging condition that can vastly exceed the experimental maximum aging time of 10 hours. Overall, there is reasonable agreement between changes in C' extracted from experimental data and those predicted by MD/MC. The modulus C' for the 1- and 10-hour aged samples increases at a decreasing rate and remains within single-digit percentages, well below the change predicted after full thermal equilibration at 500°C for the Fe-36Cr alloy. This agreement between hybrid MD/MC predictions and experimental results provides further evidence for both the magnitude and direction of the stiffening caused by spinodal decomposition in Fe-36Cr aged at 500°C.

4.3 Mechanistic explanations for spinodal stiffening

Mechanistically, spinodal decomposition can stiffen (or soften) materials through non-linearities in composition-modulus space. The effect of spinodal decomposition is separation into two phases, α and α' , which may have different elastic moduli from their parent phase, and from each other. To first order, one could use the rule of mixtures to determine the expected effect of some degree and extent of spinodal decomposition. However, non-linearities in the elastic constants of iron-chromium alloys have been shown in two studies using density functional theory [34,35]. The origin of the non-linearities were studied by Zhang et al. in ref. 35 and ascribed in large part to a strong dependence of elastic constants on the magnetic moment in binary iron-chromium alloys, which is a strong (non-linear) function of chromium composition. Additional non-linearities may arise from the very high density of phase interfaces following spinodal decomposition, though this effect is not discussed further in this manuscript.

If non-linearities exist in the elastic modulus as a function of chromium composition, spinodal decomposition could either stiffen or soften the alloy, depending on the nature of the

non-linearities and the extent and degree of spinodal decomposition. Fig. 9 shows empirical and computed values for C' from literature and this study—the key computational dataset of note is the DFT-based exact muffin-tin orbital (EMTO) computational dataset (blue circles) from ref. [34], which shows clear non-linearities in the C' modulus as a function of chromium composition, particularly in the region of interest to this study (0.2 - 0.5 atomic fraction chromium) [34]. Because inverse extraction of elastic constants from TGS is most sensitive to the C' modulus, it was chosen to compare to empirical and computed values from literature [34,36–40]. In Fig. 9 one other feature to note is that the C' modulus measured computationally by EMTO is systematically higher than C' measured experimentally. The EMTO elastic constants are static 0K results that neglect explicit phonons and finite temperature magnetic excitations. Thermal expansion, anharmonic phonons, longitudinal spin fluctuations, magnetic short-range order with non collinear moments, and dynamic spin-lattice coupling all lower C' at 298-300K, so the EMTO C' values are higher than experiments, as expected [41–46]. In terms of relative trends, however, the empirical and computational C' modulus as a function of chromium composition agree— C' generally increases as a function of chromium fraction in a non-linear fashion, with a slower rate-of-change at low chromium compositions. The slower rate of change of C' at low chromium compositions in MD compared to EMTO is because the former does not account for electronic or magnetic effects.

Two areas of note in Fig. 9 are the relative maximum in C' centered around 20 at. % chromium, where spinodal decomposition would be expected to soften the C' modulus, and the relative minimum in C' centered around 35 at. %, where spinodal would be expected to stiffen the elastic modulus. The region around 35 at. % in Fig. 9 is relevant to this study—the region highlighted in orange shows the peak and trough values of the chromium composition amplitude for the α and α' phases for the Fe-36Cr alloy aged for 10 hours at 500°C from APT data [5].

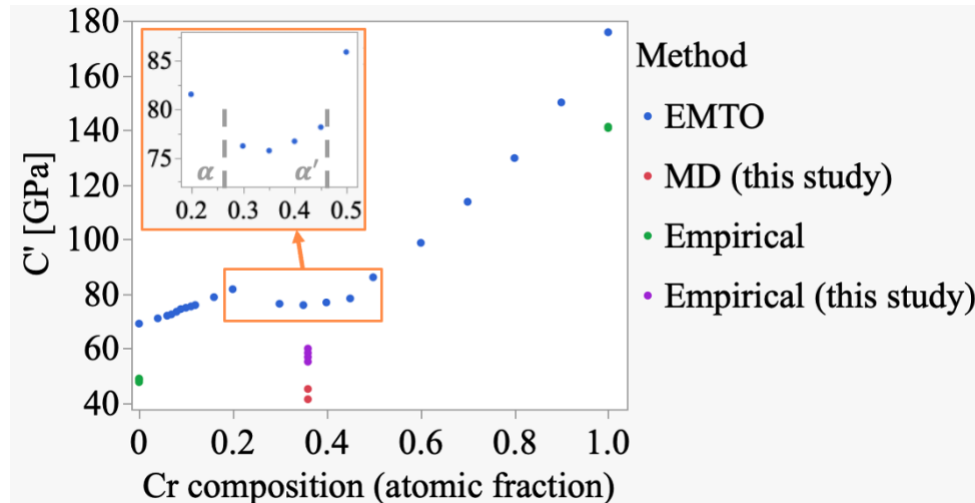


Figure 9. C' modulus as a function of chromium composition for EMTO (ref. 34) and empirical studies from literature (refs. 36–40), and from MD and TGS inverse extraction from TGS in this study.

To estimate the expected stiffening due to spinodal from the EMTO data, the amplitude (degree in units of composition) and phase fraction (extent) of α and α' must be known. The amplitude for a similarly treated Fe-36Cr alloy aged for 10 hours at 500°C was measured to be 20.1 at. % by APT (peak value of 45.9 at. % and trough value of 25.8 at. %) [5]. Phase fractions can be calculated using the lever rule—which was estimated using the iron-chromium binary phase diagram in ref. 47. The α and α' phase fractions were estimated to be 48.8% and 51.2%,

respectively. By interpolating C' values from the EMTO dataset at 25.8 and 45.9 at. % and using a simple rule of mixtures approximation, the C' modulus computed for aged alloy was 79.0 GPa, compared to 75.9 GPa for the nominal Fe-36Cr alloy. The estimated increase of 4.1% in C' after spinodal decomposition is in good agreement with the $5.4 \pm 0.5\%$ measured experimentally by TGS. It should be noted that this increase is an upper bound on the change in C' modulus at 36 at. % chromium and 500°C to the extent that the EMTO data are correct, because the calculation assumes complete phase separation into α and α' phases (i.e. an abrupt composition change at the α / α' interface), when in reality the composition change across an interface is continuous. However, this effect will lessen as spinodal decomposition proceeds, as interface density will continuously shrink following homogeneous nucleation of the two phases.

Another possible mechanism for the C' modulus increase is a change in the component of reversible elastic strain associated with pinned dislocation bowing [48]. However, the effect of stronger dislocation pinning (and thus stiffening) as the spinodal amplitude grows with time at 500°C competes with the effect of increasing spinodal wavelength, which would tend to increase the distance between pinning points and soften the modulus [49]. Though possible, the pinning effect should be mitigated by the high temperature (1100°C) annealing step in this experiment—dislocation dynamics could be used to model the effect, which is outside the scope of this study.

4.4 In-situ TGS Discussion

In-situ testing in this experiment served two primary purposes. First, to assess the ability of TGS to measure changes in elastic wave speed in-situ at temperatures where spinodal decomposition occurs. Second, to provide proof-of-concept for in-service monitoring of engineering components (e.g., duplex steels). The extensive oversampling of data from in-situ TGS also provides added confidence that the observed effects are significant and reproducible.

In “on-sample TC control”, temperature was controlled using the on-sample thermocouple, and in “in-heater TC control” temperature was controlled using the in-heater thermocouple. Temperature control via the on-sample thermocouple resulted in stability within 1°C. In contrast, when temperature was controlled using the in-heater thermocouple, the on-sample temperature continued to rise during the experiment at a rate of $\sim 1.5^\circ\text{C}/\text{hour}$.

Poor temperature accuracy and control has two main effects. First, a temperature increase softens the elastic modulus of the Fe-36Cr sample, resulting in a decrease in the elastic wave speed. Second, because the kinetics of spinodal decomposition are temperature-dependent, accurate and stable temperature control is required to compare in-situ and ex-situ results. The positive rate of temperature rise for the in-heater TC control produces competing effects: modulus softening from the temperature rise and modulus stiffening from spinodal decomposition. In future experiments, temperature should be controlled exclusively via the on-sample thermocouple.

Beyond temperature control, three characteristics of the in-situ TGS data in Fig. 5 stand out. First, there is clear stiffening in both alloys as a function of time at temperatures where spinodal decomposition is expected in the Fe-36Cr alloy. This observation is consistent with ex-situ results and demonstrates that TGS can detect stiffening in-situ. Second, the initial SAW speed for in-heater TC control starts lower than the on-sample TC control case, but increases less on a percentage basis. Although this appears inconsistent with ex-situ data, it is likely due to the competing effect of temperature increase, which softens the Fe-36Cr modulus and SAW speed. Finally, approximately one hour into both in-situ experiments, the rate of stiffening decreases significantly, as shown in Fig. 5. For in-heater TC control, the rate of stiffening after ~ 1 hour appears to approach zero. This effect may result from the increasing temperature,

which softens the material over time, counteracting the stiffening from spinodal decomposition. The change in slope after ~1 hour suggests a shift in the kinetics of spinodal decomposition, consistent with in-situ, time-resolved small-angle neutron (SANS) scattering data on spinodal progression in Fe-Cr alloys [11].

Hörnqvist et al. performed an in-situ SANS experiment on an Fe-36.9Cr (at. %) alloy aged for 10 hours at 500°C [11]. Before 1 hour at 500°C, the characteristic distance (analogous to the spinodal wavelength) oscillated around the expected power-law behavior predicted by the Cahn-Hilliard-Cook model. After 1 hour, the characteristic distance followed the expected power-law growth with time [11]. Both in-situ SANS and in-situ TGS reveal a distinct change in the progression of spinodal decomposition after ~1 hour of aging at 500°C for Fe-36Cr alloys. Although TGS measures the elastic effects of spinodal decomposition at the mesoscale while SANS probes nanoscale changes in atomic ordering, the agreement in kinetic behavior demonstrates that TGS is sufficiently sensitive to track small changes in the progression of spinodal decomposition.

In the on-sample TC control case, the kinetic change occurs at approximately 65 minutes into the experiment. Before the 65-minute mark, the average slope is 0.47 m/s/min; after, it decreases to 0.09 m/s/min. Given that TGS can detect changes on the order of 0.1% of the mean SAW speed, the slope change should be statistically significant after ~6 minutes in the on-sample TC control case. The in-heater TC control data, however, exhibit greater variability, which would increase the time required to identify a statistically significant change—the time resolution for in-heater TC control to track kinetic changes was ~3 times worse than for on-sample TC control. The ability of TGS to track kinetic changes in situ also depends on the magnitude of the slope change in SAW speed during the process, which may vary with the kinetic mechanism and the angular SAW dispersion in each grain. In this case, TGS was sufficiently sensitive to track the kinetic process in-situ. Beyond the slope change, the absolute change in SAW speed for the on-sample TC control in-situ measurement was about 50 ± 2.1 m/s, or 1.8%, which is much larger than the detection limit of TGS. This provides strong evidence that TGS can measure stiffening due to spinodal decomposition in binary iron-chromium alloys.

The ability of in-situ TGS to detect stiffening enables the potential for in-service monitoring of structural components. In a commercial system, two emerging TGS technologies could be integrated for in-operando detection of spinodal decomposition. First, a small area ($\sim 0.5 \times 0.5$ cm) on the part must be polished to a mirror-finish. Second, a compact TGS system can be attached to the part [50]. Third, a map of the polished area can be obtained using the compact TGS system, with measurements spanning several grains and possibly multiple grating directions (by rotating the compact stage) [51]. Repeated mapping over time, combined with automated analysis, could track stiffening and correlate it to the progression of spinodal decomposition. There are no scientific obstacles to realizing such an in-operando TGS system—existing technologies simply need to be integrated into a single, portable system.

5. Conclusion

The results presented demonstrate the stiffening effect of spinodal decomposition in Fe-36Cr is measurable by both in-situ and ex-situ TGS. The binary nature of the Fe-Cr alloys in this study eliminates competing effects observed in more complex CASS alloys, particularly G-phase precipitation. DSC provides evidence of spinodal decomposition in the Fe-36Cr alloy, and hybrid MD/MC results show agreement with experimental measurements on the extent of Fe-36Cr stiffening caused by spinodal decomposition.

TGS was shown to be sufficiently sensitive to measure SAW speed changes in the Fe-36Cr alloy under the time-at-temperature aging conditions used in this study, though it was not

sensitive enough to resolve changes in the Fe-26Cr alloy. In general, SAW speed changes on the order of 0.1% are measurable, and the in-situ experiments confirmed that this level of sensitivity is sufficient to track kinetic changes associated with spinodal decomposition in Fe36-Cr.

TGS is a relatively inexpensive, non-destructive technique capable of accurately tracking elastic properties both in- and ex-situ. Developing a commercial TGS system for in-operando monitoring would require the integrating recent advances in TGS mapping and miniaturization, along with carefully controlled component tests over extended time periods. Although some engineering challenges remain to realize such a system, little scientific uncertainty remains.

Acknowledgments

The authors would like to convey sincere thanks to Linn Hobbs for providing the Fe-26Cr sample. We gratefully acknowledge Prof. Craig Carter for guidance and assistance in computing the characteristic spinodal wavelength. M.I. acknowledges support from the MathWorks Engineering Fellowship Fund. Atomistic simulations were performed using the Expanse supercomputer at the San Diego Supercomputer Center through allocation MAT210005 from the Advanced Cyberinfrastructure Coordination Ecosystem: Services & Support (ACCESS) program, supported by National Science Foundation grants #2138259, #2138286, #2138307, #2137603, and #2138296. Additional computational resources were provided by the Extreme Science and Engineering Discovery Environment (XSEDE), supported by National Science Foundation grant #1548562. Throughout the duration of this work, S.A.A. was funded by the King Abdullah University of Science and Technology (KAUST) Fellowship and the MIT Department of Civil and Environmental Engineering (CEE) under the Friescke (1961) Fellowship Fund. K.R. and T.G. acknowledge support from Czech Science Foundation [project No. 22-13462S] and from the project FerrMion [project No. CZ.02.01.01/00/22_008/0004591] of the Czech Ministry of Education, Youth, and Sports, co-funded by the European Union.

Declaration of generative AI and AI-assisted technologies in the manuscript preparation process

Generative AI and AI-assisted technologies were not used for the preparation of this manuscript.

References

- [1] B. Robert W., A. Samuel M., C. Craig W., 17.3 Classification of Phase Transformations: Continuous Versus Discontinuous Transformations, in: Kinetics of Materials, John Wiley & Sons, Inc., 2005: pp. 430–431.
- [2] T.S. Byun, Y. Yang, N.R. Overman, J.T. Busby, Thermal Aging Phenomena in Cast Duplex Stainless Steels, *JOM* 68 (2016) 507–516. <https://doi.org/10.1007/s11837-015-1709-9>.
- [3] G. Obulan Subramanian, B.S. Kong, H.J. Lee, C. Jang, Evaluation of the thermal aging of δ -ferrite in austenitic stainless steel welds by electrochemical analysis, *Sci Rep* 8 (2018) 15091. <https://doi.org/10.1038/s41598-018-33422-x>.
- [4] J.E. Westraadt, E.J. Olivier, J.H. Neethling, P. Hedström, J. Odqvist, X. Xu, A. Steuwer, A high-resolution analytical scanning transmission electron microscopy study of the early stages of spinodal decomposition in binary Fe–Cr, *Materials Characterization* 109 (2015) 216–221. <https://doi.org/10.1016/j.matchar.2015.10.001>.
- [5] J. Zhou, J. Odqvist, M. Thuvander, P. Hedström, Quantitative Evaluation of Spinodal Decomposition in Fe–Cr by Atom Probe Tomography and Radial Distribution Function Analysis, *Microsc Microanal* 19 (2013) 665–675. <https://doi.org/10.1017/S1431927613000470>.
- [6] F. Danoix, P. Auger, Atom Probe Studies of the Fe–Cr System and Stainless Steels Aged at Intermediate Temperature, *Materials Characterization* 44 (2000) 177–201. [https://doi.org/10.1016/S1044-5803\(99\)00048-0](https://doi.org/10.1016/S1044-5803(99)00048-0).
- [7] X. Xu, J. Odqvist, M.H. Colliander, M. Thuvander, A. Steuwer, J.E. Westraadt, S. King, P. Hedström, Structural Characterization of Phase Separation in Fe–Cr: A Current

Comparison of Experimental Methods, *Metall Mater Trans A* 47 (2016) 5942–5952. <https://doi.org/10.1007/s11661-016-3800-4>.

[8] W. Xiong, P. Hedström, M. Selleby, J. Odqvist, M. Thuvander, Q. Chen, An improved thermodynamic modeling of the Fe–Cr system down to zero kelvin coupled with key experiments, *Calphad* 35 (2011) 355–366. <https://doi.org/10.1016/j.calphad.2011.05.002>.

[9] W. Xiong, M. Selleby, Q. Chen, J. Odqvist, Y. Du, Phase Equilibria and Thermodynamic Properties in the Fe–Cr System, *Critical Reviews in Solid State and Materials Sciences* 35 (2010) 125–152. <https://doi.org/10.1080/10408431003788472>.

[10] M.K. Miller, J.M. Hyde, M.G. Hetherington, A. Cerezo, G.D.W. Smith, C.M. Elliott, Spinodal decomposition in Fe–Cr alloys: Experimental study at the atomic level and comparison with computer models—I. Introduction and methodology, *Acta Metallurgica et Materialia* 43 (1995) 3385–3401. [https://doi.org/10.1016/0956-7151\(95\)00040-3](https://doi.org/10.1016/0956-7151(95)00040-3).

[11] M. Hörnqvist, M. Thuvander, A. Steuwer, S. King, J. Odqvist, P. Hedström, Early stages of spinodal decomposition in Fe–Cr resolved by *in-situ* small-angle neutron scattering, *Applied Physics Letters* 106 (2015) 061911. <https://doi.org/10.1063/1.4908250>.

[12] R. Badyka, G. Monnet, S. Sallet, C. Domain, C. Pareige, Quantification of hardening contribution of G-Phase precipitation and spinodal decomposition in aged duplex stainless steel: APT analysis and micro-hardness measurements, *Journal of Nuclear Materials* 514 (2019) 266–275. <https://doi.org/10.1016/j.jnucmat.2018.12.002>.

[13] H.M. Chung, Aging and life prediction of cast duplex stainless steel components, *International Journal of Pressure Vessels and Piping* 50 (1992) 179–213. [https://doi.org/10.1016/0308-0161\(92\)90037-G](https://doi.org/10.1016/0308-0161(92)90037-G).

[14] S.A.A. Al Dajani, B.R. Dacus, C.A. Dennett, M.G. Burke, L. Waldron, T.S. Byun, J.J. Wall, K.B.-D. Anglin, O.A.A. Al Dajani, K.J. Krakowiak, Franz.-J. Ulm, A. Schwartzmann, C.C. Tasan, P. Hosemann, M.P. Short, Detecting Thermally-Induced Spinodal Decomposition with Picosecond Ultrasonics in Cast Austenitic Stainless Steels, *Acta Materialia* 246 (2023) 118552. <https://doi.org/10.1016/j.actamat.2022.118552>.

[15] F. Hofmann, M.P. Short, C.A. Dennett, Transient grating spectroscopy: An ultrarapid, nondestructive materials evaluation technique, *MRS Bull.* 44 (2019) 392–402. <https://doi.org/10.1557/mrs.2019.104>.

[16] P. Stoklasová, P. Sedláček, H. Seiner, M. Landa, Forward and inverse problems for surface acoustic waves in anisotropic media: A Ritz–Rayleigh method based approach, *Ultrasonics* 56 (2015) 381–389. <https://doi.org/10.1016/j.ultras.2014.09.004>.

[17] M. Rae, M. Islam, M.P. Short, Data repository for Max’s manuscript on detecting spinodal decomposition using TGS, (n.d.). <https://github.com/shortlab/2025-mraechu-spinodal-is-real> (accessed November 1, 2025).

[18] P. Stoklasová, T. Grabec, K. Zoubková, P. Sedláček, S. Krátký, H. Seiner, Laser-Ultrasonic Characterization of Strongly Anisotropic Materials by Transient Grating Spectroscopy, *Exp Mech* 61 (2021) 663–676. <https://doi.org/10.1007/s11340-021-00698-6>.

[19] Y. Li, L. Zhu, C. Liu, S. Shi, Nanoscale Phase Evolution during Continuum Decomposition of Fe–Cr Alloys, *Materials* 10 (2017) 1431. <https://doi.org/10.3390/ma10121431>.

[20] C.A. Hirst, F. Granberg, B. Kombaiah, P. Cao, S. Middlemas, R.S. Kemp, J. Li, K. Nordlund, M.P. Short, Revealing hidden defects through stored energy measurements of radiation damage, *Sci. Adv.* 8 (2022) eabn2733. <https://doi.org/10.1126/sciadv.abn2733>.

[21] L. Couturier, F. De Geuser, A. Deschamps, A comparative study of Fe-Cr unmixing using differential scanning calorimetry and small-angle scattering, *Materials Characterization* 173 (2021) 110934. <https://doi.org/10.1016/j.matchar.2021.110934>.

[22] L. Couturier, F. De Geuser, A. Deschamps, Microstructural evolution during long time aging of 15–5PH stainless steel, *Materialia* 9 (2020) 100634. <https://doi.org/10.1016/j.mtla.2020.100634>.

[23] A.P. Thompson, H.M. Aktulga, R. Berger, D.S. Bolintineanu, W.M. Brown, P.S. Crozier, P.J. In 'T Veld, A. Kohlmeyer, S.G. Moore, T.D. Nguyen, R. Shan, M.J. Stevens, J. Tranchida, C. Trott, S.J. Plimpton, LAMMPS - a flexible simulation tool for particle-based materials modeling at the atomic, meso, and continuum scales, *Computer Physics Communications* 271 (2022) 108171. <https://doi.org/10.1016/j.cpc.2021.108171>.

[24] S.M. Eich, D. Beinke, G. Schmitz, Embedded-atom potential for an accurate thermodynamic description of the iron–chromium system, *Computational Materials Science* 104 (2015) 185–192. <https://doi.org/10.1016/j.commatsci.2015.03.047>.

[25] N. Metropolis, A.W. Rosenbluth, M.N. Rosenbluth, A.H. Teller, E. Teller, Equation of state calculations by fast computing machines, 1953. <https://doi.org/10.2172/4390578>.

[26] W.K. Hastings, Monte Carlo sampling methods using Markov chains and their applications, *Biometrika* 57 (1970) 97–109. <https://doi.org/10.1093/biomet/57.1.97>.

[27] G. Clavier, N. Desbiens, E. Bourasseau, V. Lachet, N. Brusselle-Dupend, B. Rousseau, Computation of elastic constants of solids using molecular simulation: comparison of constant volume and constant pressure ensemble methods, *Molecular Simulation* 43 (2017) 1413–1422. <https://doi.org/10.1080/08927022.2017.1313418>.

[28] A. Stukowski, Visualization and analysis of atomistic simulation data with OVITO—the Open Visualization Tool, *Modelling Simul. Mater. Sci. Eng.* 18 (2010) 015012. <https://doi.org/10.1088/0965-0393/18/1/015012>.

[29] S.S. Brenner, P.P. Camus, M.K. Miller, W.A. Soffa, Phase separation and coarsening in Fe-Cr-Co alloys, *Acta Metallurgica* 32 (1984) 1217–1227. [https://doi.org/10.1016/0001-6160\(84\)90128-7](https://doi.org/10.1016/0001-6160(84)90128-7).

[30] M. Oehring, L. v. Alvensleben, EVALUATION OF ATOM PROBE CONCENTRATION PROFILES BY AUTOCORRELATION ANALYSIS, *J. Phys. Colloques* 49 (1988) C6-415-C6-420. <https://doi.org/10.1051/jphyscol:1988671>.

[31] J.S. Langer, M. Bar-on, H.D. Miller, New computational method in the theory of spinodal decomposition, *Phys. Rev. A* 11 (1975) 1417–1429. <https://doi.org/10.1103/PhysRevA.11.1417>.

[32] M.K. Miller, Atom Probe Tomography: Analysis at the Atomic Level, *Journal of Microscopy* 201 (2001) 417–418. <https://doi.org/10.1046/j.1365-2818.2001.00847.x>.

[33] D.J. Seol, S.Y. Hu, Y.L. Li, J. Shen, K.H. Oh, L.Q. Chen, Computer simulation of spinodal decomposition in constrained films, *Acta Materialia* 51 (2003) 5173–5185. [https://doi.org/10.1016/S1359-6454\(03\)00378-1](https://doi.org/10.1016/S1359-6454(03)00378-1).

[34] V.I. Razumovskiy, A.V. Ruban, P.A. Korzhavyi, First-principles study of elastic properties of Cr- and Fe-rich Fe-Cr alloys, *Phys. Rev. B* 84 (2011) 024106. <https://doi.org/10.1103/PhysRevB.84.024106>.

[35] H. Zhang, G. Wang, M.P.J. Punkkinen, S. Hertzman, B. Johansson, L. Vitos, Elastic anomalies in Fe–Cr alloys, *J. Phys.: Condens. Matter* 25 (2013) 195501. <https://doi.org/10.1088/0953-8984/25/19/195501>.

[36] D.I. Bolef, J. De Klerk, Anomalies in the Elastic Constants and Thermal Expansion of Chromium Single Crystals, *Phys. Rev.* 129 (1963) 1063–1067. <https://doi.org/10.1103/PhysRev.129.1063>.

[37] A. Sumer, J.F. Smith, A Comparison of the Elastic Constants of Chromium as Determined from Diffuse X-Ray and Ultrasonic Techniques, *Journal of Applied Physics* 34 (1963) 2691–2694. <https://doi.org/10.1063/1.1729792>.

[38] H.M. Ledbetter, R.P. Reed, Elastic Properties of Metals and Alloys, I. Iron, Nickel, and Iron-Nickel Alloys, *Journal of Physical and Chemical Reference Data* 2 (1973) 531–618. <https://doi.org/10.1063/1.3253127>.

[39] J.A. Rayne, B.S. Chandrasekhar, Elastic Constants of Iron from 4.2 to 300°K, *Phys. Rev.* 122 (1961) 1714–1716. <https://doi.org/10.1103/PhysRev.122.1714>.

[40] D.J. Dever, Temperature dependence of the elastic constants in α -iron single crystals: relationship to spin order and diffusion anomalies, *Journal of Applied Physics* 43 (1972) 3293–3301. <https://doi.org/10.1063/1.1661710>.

[41] Z. Dong, W. Li, S. Schönecker, S. Lu, D. Chen, L. Vitos, Thermal spin fluctuation effect on the elastic constants of paramagnetic Fe from first principles, *Phys. Rev. B* 92 (2015) 224420. <https://doi.org/10.1103/PhysRevB.92.224420>.

[42] J.B.J. Chapman, P.-W. Ma, S.L. Dudarev, Dynamics of magnetism in Fe-Cr alloys with Cr clustering, *Phys. Rev. B* 99 (2019) 184413. <https://doi.org/10.1103/PhysRevB.99.184413>.

[43] R. Soulairol, C. Barreteau, C.-C. Fu, Interplay between magnetism and energetics in Fe-Cr alloys from a predictive noncollinear magnetic tight-binding model, *Phys. Rev. B* 94 (2016) 024427. <https://doi.org/10.1103/PhysRevB.94.024427>.

[44] X. Li, S. Schönecker, J. Zhao, L. Vitos, B. Johansson, Elastic anharmonicity of bcc Fe and Fe-based random alloys from first-principles calculations, *Phys. Rev. B* 95 (2017) 024203. <https://doi.org/10.1103/PhysRevB.95.024203>.

[45] D. Perera, D.P. Landau, D.M. Nicholson, G. Malcolm Stocks, M. Eisenbach, J. Yin, G. Brown, Phonon-magnon interactions in body centered cubic iron: A combined molecular and spin dynamics study, *Journal of Applied Physics* 115 (2014) 17D124. <https://doi.org/10.1063/1.4863488>.

[46] H. Zhang, C. Li, P. Djemia, R. Yang, Q. Hu, Prediction on temperature dependent elastic constants of “soft” metal Al by AIMD and QHA, *Journal of Materials Science & Technology* 45 (2020) 92–97. <https://doi.org/10.1016/j.jmst.2019.11.029>.

[47] O. Kubaschewski, *IRON-Binary Phase Diagrams*, Springer Berlin Heidelberg Imprint: Springer, Berlin, Heidelberg s.l, 1982. <https://doi.org/10.1007/978-3-662-08024-5>.

[48] J. Friedel, Anomaly in the rigidity modulus of copper alloys for small concentrations, *The London, Edinburgh, and Dublin Philosophical Magazine and Journal of Science* 44 (1953) 444–448. <https://doi.org/10.1080/14786440408520327>.

[49] J. Friedel, N. Kurti, R. Smoluchowski, *Dislocations*, Elsevier Science, n.d.

[50] J. Rajagopal, A.P.C. Wylie, B. Dacus, T. St. Julian, M.P. Short, A compact, asymmetric probe, planar transient grating spectroscopy system, *Review of Scientific Instruments* 96 (2025) 033001. <https://doi.org/10.1063/5.0233331>.

[51] C. Weaver, M. Stapelberg, M.P. Short, A. Wylie, E.B. Artalejo, Automated transient grating spectroscopy mapping and signal control for large samples, *Review of Scientific Instruments* 95 (2024) 074902. <https://doi.org/10.1063/5.0202262>.